GPS-based ionospheric tomography with a constrained adaptive simultaneous algebraic reconstruction technique

Wen Debao[1,*], Zhang Xiao[1], Tong Yangjin[1], Zhang Guangsheng[2], Zhang Min[1] and Leng Rusong[1]

[1]*School of Traffic and Transportation Engineering, Changsha University of Science & Technology, Changsha 410004, China.*
[2]*School of Surveying and Land Information Engineering, Henan Polytechnic University, Jiaozuo 454000, China.*
[*]*Corresponding author. e-mail: wdbwhigg@163.com*

In this paper, a constrained adaptive simultaneous algebraic reconstruction technique (CASART) is presented to obtain high-quality reconstructions from insufficient projections. According to the continuous smoothness of the variations of ionospheric electron density (IED) among neighbouring voxels, Gauss weighted function is introduced to constrain the tomography system in the new method. It can resolve the dependence on the initial values for those voxels without any GPS rays traversing them. Numerical simulation scheme is devised to validate the feasibility of the new algorithm. Some comparisons are made to demonstrate the superiority of the new method. Finally, the actual GPS observations are applied to further validate the feasibility and superiority of the new algorithm.

1. Introduction

In recent years, ionospheric tomography has been introduced as a new monitoring technique in the ionospheric field. The technique is applied to reconstruct the three-dimensional distribution of IED using the total electron content (TEC) measurements from various GPS ray paths (Escudero *et al.* 2001; Mitchell and Spencer 2003; Ma and Maruyama 2005; Stoll *et al.* 2006; Yizengaw *et al.* 2007; Li *et al.* 2012). It is advantageous to overcome the limitations associated with 2D ionospheric models and direct measuring technique, such as *in-situ* electron density measurements, which give only localized information at any time and location (Fredman and Nickisch 2001; Kunitsyn *et al.* 2010). At present, GPS-based ionospheric tomography is the research focus in the fields of space geodesy and space physics since it can be used to reconstruct the three-dimensional variation information of the ionosphere. This is very useful for the development of GNSS such as GPS, Glonass, Galileo and Compass, as these systems are affected by the variations of IED, particularly those variations that do not follow a regular predictable pattern (Thampi *et al.* 2004; Gracia and Crespon 2008; Lee and Kamalabadi 2009; Nesterov and Kunitsyn 2011; Yao *et al.* 2013).

Unlike the computerized tomography in medical field, the available GPS observations are usually insufficient in ionospheric tomography due to the limited number of observation stations and finite receiving apertures (Persson *et al.* 2001). However, high-resolution 3D image reconstruction requires a method that can be used to deal with the insufficiency of the observation data (Thampi *et al.* 2004). Due to its algorithmic simplicity and computational efficiency, adaptive simultaneous algebraic

Keywords. Ionospheric tomography; Gauss weighted function; electron density; constrained adaptive simultaneous algebraic reconstruction technique; GPS.

reconstruction technique (ASART) has been one of the attractive methods in the image reconstruction (Wan *et al.* 2011). The major disadvantage of ASART, however, is that the results may be strongly affected by limited angle data. For those voxels which have any GPS rays traversing them, the final results of ASART are strongly dependent on the initial values given by empirical ionospheric models, such as IRI 2007. However, empirical models reflect the monthly average effect of the ionosphere; it severely limits the accuracy of the tomographic results of IED (Wen *et al.* 2007). To resolve the above problem, CASART algorithm is presented in this paper. Taking the continuous smoothness of the variations of IED among neighbouring voxels into account, Gauss weighted function is introduced to constrain the tomography system in the new method. Better images can be reconstructed by the new method using much fewer measurements than the traditional computerized ionospheric tomography. Numerical experiments validate the feasibility and reliability, some comparisons are made to confirm the advantageous of the new method.

2. Ionospheric tomography technique

In ionospheric tomography, the available projections are the slant TEC measurements, which are the integral of IED between satellite-receiver ray paths. The integral equation has been given by Austen *et al.* (1988).

$$\mathrm{STEC} = \int_{r_i}^{s^j} N_e\,(s,t)\,ds \tag{1}$$

for $i = 1, 2, ..., I$, $j = 1, 2, ..., J$, where N_e is the electron density, t is the time, s is the path along the satellite-to-receiver ray path, I and J are the number of receivers and satellites, and r_i and s^j are the receiver and satellite positions, respectively.

Because the problem is numerically solved, the integration over the paths in equation (1) is performed over voxels of a certain size, modifying the equation as:

$$\mathrm{STEC} = \sum_{j=1}^{n} A_{ij}x_j + e_i. \tag{2}$$

Equation (2) is generally expressed in a simple matrix notation as:

$$\boldsymbol{y}_{m\times 1} = \boldsymbol{A}_{m\times n}\boldsymbol{x}_{n\times 1} + \boldsymbol{e}_{m\times 1} \tag{3}$$

where n is the number of voxels in the image region, m is the number of slant TEC measurements, $\boldsymbol{y}$ is a column vector of the m known TEC measurements, $\boldsymbol{A}$ is a matrix containing all the lengths of the m ray paths traversing the corresponding n voxels, $\boldsymbol{x}$ is the vector consisting of all the unknown electron densities of all the voxels, and $\boldsymbol{e}$ is a column vector associated with the discretization errors and measurement noises.

3. A constrained ASART

Due to higher-quality reconstruction, faster convergence and less artifacts, ASART is very attractive to the image reconstruction when computer memory is limited. The procedure has been described by Wan *et al.* (2011), which can be represented as:

$$x_j^{(k+1)} = x_j^{(k)} + \sum_{i=1}^{m} \frac{\gamma A_{ij}}{\sum_{i=1}^{m} A_{ij}\cdot\sum_{j=1}^{n} A_{ij}}\left(y_i - A_i x^{(k)}\right),$$
$$\lambda_k = \frac{\gamma A_{ij}x_j^{(k)}}{\sum_{i=1}^{m} A_{ij}\cdot\sum_{j=1}^{n} A_{ij}x_j^{(k)}}. \tag{4}$$

The symbol A_i represents the ith row vector in projection matrix A, γ is called relaxation factor which is a constant $(0 < \lambda < 2)$, k is the number of iterations, λ_k is the relaxation parameter, $x_j^{(k+1)}$ is the next iterative value updated by$x_j^{(k)}$.

As the above descriptions, in the GPS-based ionospheric tomography, the projected slant TEC data is constrained into a small angle range, which is almost in perpendicular direction. Moreover, the number of ground receivers is limited and not evenly distributed. For those voxels without any ray paths traversing them, the final results are equal to the initial values when ASART is used to reconstruct the IED distribution. However, the initial values are usually obtained from empirical ionospheric models. This makes the results inconsistent with the reality.

In general, the variation of IED is smooth and continuous. According to the principle that, relativity increases with the descending of the distance, Gauss weighting function is used for horizontal constraints, so the constraint equation is given as:

$$w_1x_1 + \cdots + w_{j-1}x_{j-1} - x_j + w_{j+1}x_{j+1} + \cdots = 0 \tag{5}$$

when the ith voxel does not lie the same layer with the jth voxel, so $w_i = 0$, on the contrary, the weight coefficient can be computed using the following equation

$$w_i = \frac{e^{-(d_{i,j}^2/2\sigma^2)}}{\sum_{i_1=1}^{ne}\sum_{j_1=1}^{nn} e^{-(d_{i,j}^2/2\sigma^2)}} \tag{6}$$

where ne and nn are the number of voxels in the longitude and latitude direction, respectively, $d_{i,j}$

is the distance between the ith voxel and the jth voxel, and σ is the smoothing operator.

4. Numerical experiments

4.1 *Experiment 1 (using simulated data)*

In this work, the objective is to improve the quality of IED tomographic reconstruction image. The advantageous of CASART is confirmed by comparing the imaging quality between the CASART and the ASART. Before applying CASART to perform the reconstruction of IED distribution, it is also necessary to validate the feasibility and reliability of the new algorithm. For this purpose, a numerical simulation is first carried out. The reconstructed range in latitude is selected from 19° to 27°N for 01:30-02:00UT, May 8, 2012. The longitude ranges from 108° to 112°E. The height range is probably 100 to 1000 km. The discretized intervals in latitude and longitude directions are 0.5°. In the height, the step is 10 km. In this scheme, the simulated IED at the center of each voxel is generated from the IRI 2007 model and considered as the initial electron density value of the corresponding voxel. The distribution is represented by x_{simu}, and then the simulated TEC measurement y_{simu} without noise is computed by using the following equation

$$y_{\text{simu}} = A \cdot x_{\text{simu}}. \tag{7}$$

Taking the fact into account, a small amount of random noise e_{simu} should be added to the simulated TEC values y_{simu}. The maximum noise is 5% of the average value of the simulated TEC data in this work. The slant TEC with noise can be written as:

$$y_{\text{nois}} = y_{\text{simu}} + e_{\text{simu}}. \tag{8}$$

In addition, precise known positions of GPS satellites and 23 ground receivers located in the selected geographic region during the interest time period are used to obtain coefficient matrix A. The initial IED values, which are needed to perform the CASART and the ASART, are set to 0.8 times of the above IED distributions.

Figure 1(a) illustrates the IED distributions along 110°E, which is obtained from the IRI 2007 model. The tomographic reconstruction of IED distributions using the ASART and the CASART are shown in figure 1(b and c), respectively. Comparing figure 1(c) with figure 1(a), it can be seen that the ionospheric structure is reconstructed well as a whole. This result confirms the feasibility of the IED reconstruction using the CASART. However, figure 1(b) shows that the imaging quality of the ASART is poorer than that of the CASART. It validates the superiority of the CASART to the ASART in the process of CIT.

Figure 2(a and b) shows the IED reconstructed error comparisons of all the voxels along 110°E using the ASART and the CASART, respectively. From figure 2(b), it can be seen that the maximum absolute value of the IED reconstructed errors is smaller than that of shown in figure 2(a), and that the voxel numbers with smaller errors is obviously increased. The comparison validates that the reconstructed accuracy of the CASART is better than that of the ASART.

4.2 *Experiment 2 (real GPS data)*

The feasibility and superiority of the new algorithm are first validated using simulated slant TEC data. To further demonstrate the new algorithm, it is necessary to use the real GPS data to reconstruct IED distributions. The dual-frequency GPS data of 114 stations from the Crustal Movement Observation Network of China (CMONC) are applied to investigate the effects of the diurnal variations of IED distribution. The selected ground-based GPS stations are shown in figure 3. Before the reconstruction of IED, each voxel in the reconstruction region is initialized by the IRI 2007 model. Then the iteration is carried out by the new algorithm.

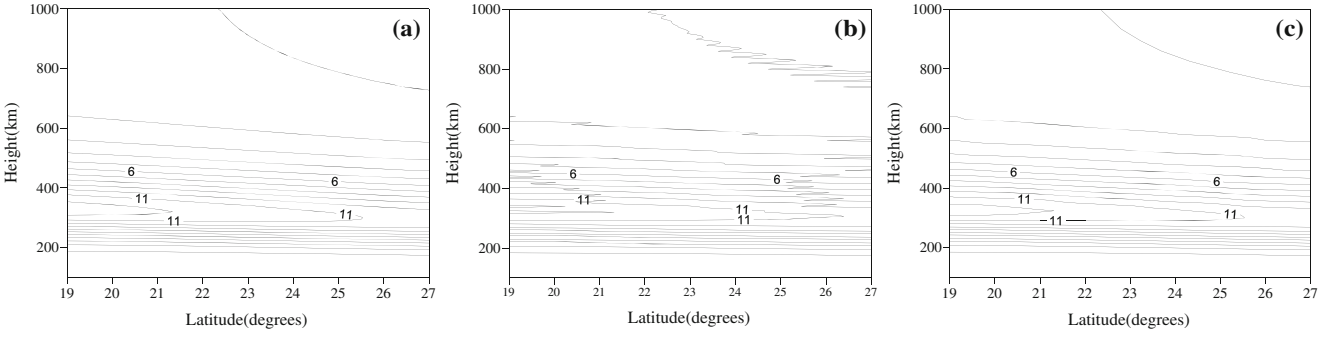

Figure 1. Contour plots of the IRI 2007 and the reconstructed IED distributions along 110°E using the ASART and the CASART. **(a)** IRI 2007; **(b)** ASART; **(c)** CASART (IED is in unit of 10^{11}el/m^3).

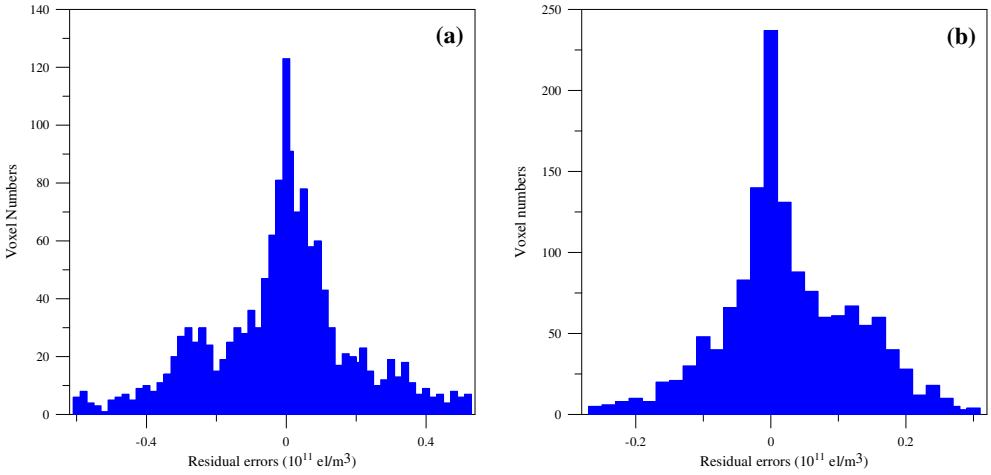

Figure 2. Comparison of the reconstructed errors of the ASART and CASART along 110°E. **(a)** ASART and **(b)** CASART.

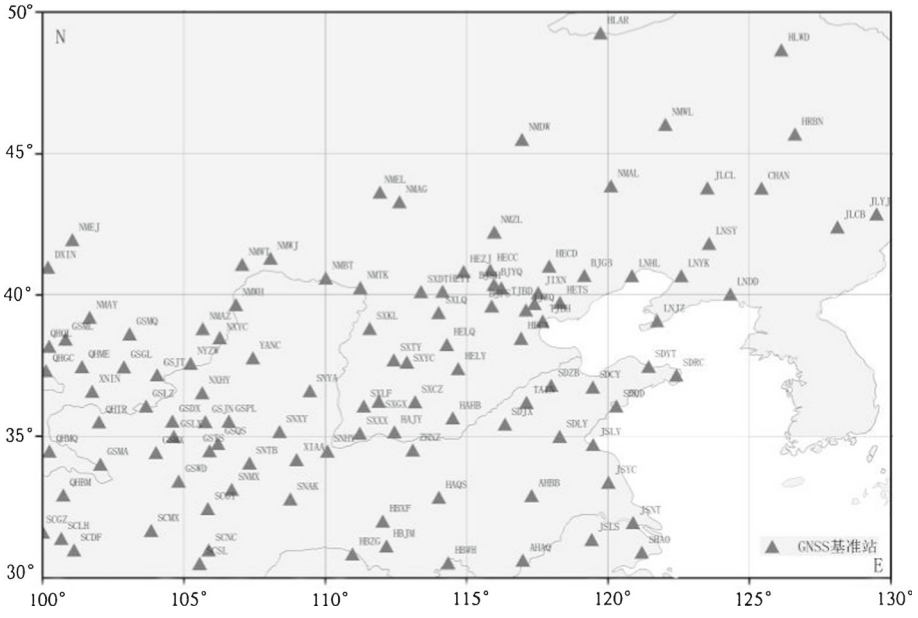

Figure 3. Sketch map of the selected ground-based GPS observation stations.

Figure 4 illustrates the evolution of the ionosphere over China on March 1, 2012. The tomographic reconstruction is carried out for a whole day with different-time sampling. Each snapshot is plotted with respect to latitude and height at the meridian plane at 114°E. From figure 4(a–c), it can be seen that the peak height of the ionosphere first rises from 260 to 300 km, and then the height falls from 300 to 280 km. At 13:00UT, the peak height of the IED gradually rises and reaches 320 km. It always remains about the same height in the night. The results roughly reflect typical characteristics of the vertical variations of the ionospheric structure for the day over China.

Figure 5 shows that the time-series variation of IED as the latitude and longitude at the height of 350 km over China. From this figure, it can be seen that the inverted average IED values grow from small to large first, and then fall from large to small, which is consistent with the Earth's rotation from west to east. This is also consistent with the normal change laws in daytime and night time over China as well as the fact that the characteristics of IED depends mainly on the solar activity. Furthermore, it can also be seen that the values of IED in eastern China are larger than those in western China between 01:00 UT and 05:00 UT, and then the values of IED in western China are larger than those in eastern China between 09:00 UT and 17:00 UT as a whole. However, at 23:00 UT, the values of IED in eastern China begin to increase, and the values of IED in eastern China are larger than those in western China.

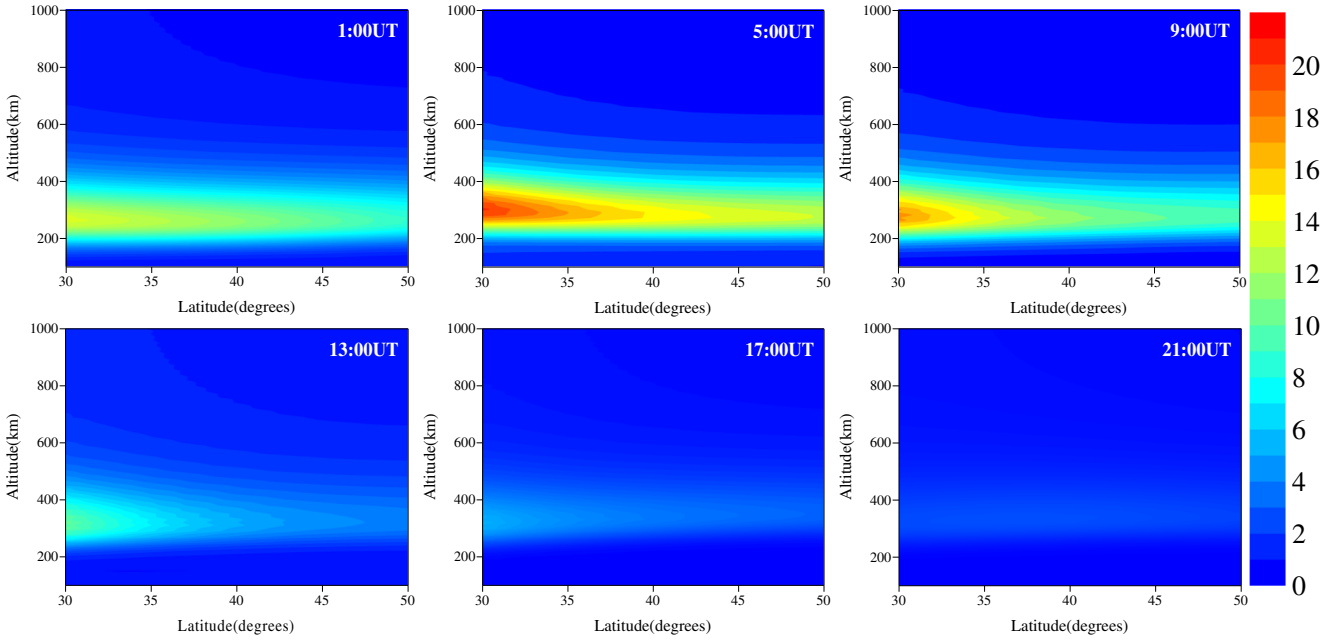

Figure 4. Time-series sample images of IED at 114°E on March 1, 2012. The time for each panel is given at the top right corner. The unit of the colour bar is 10^{11} el/m^3.

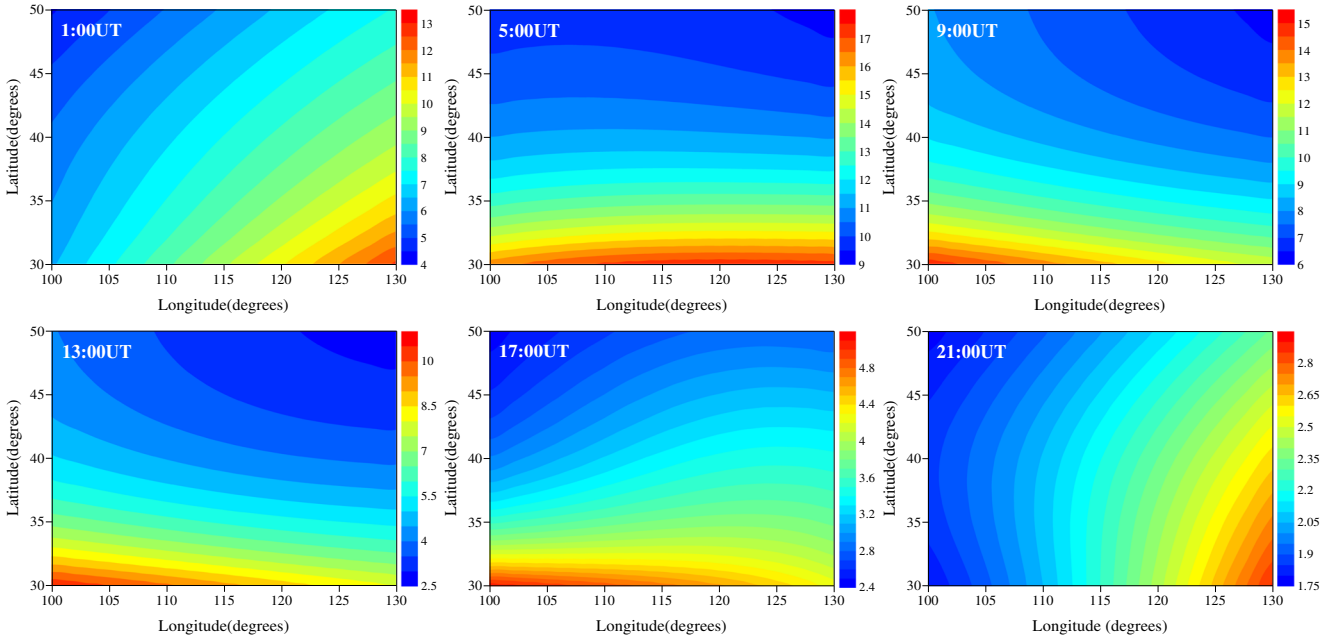

Figure 5. Time-series variations of ionospheric electron density at the height of 350 km on March 1, 2012. The unit of the colour bar is 10^{11} el/m^3.

Figures 4 and 5 also show that there are larger differences between the characteristics of the IED in mid-latitude and low-latitude areas, and the values of IED over northern China are smaller than those over southern China as a whole. This indicates a strong correlation of the variation of IED with latitude. The maximum and the minimum IED occurs at 5:00UT and 21:00UT, respectively.

To demonstrate superiority of the CASART to the ASART method and the IRI 2007 model, the ionospheric electron density distributions reconstructed from the above two methods and the IRI 2007 are compared with the ionosonde data, and the differences between the reconstructed results and the recorded ionosonde data are obtained. In this work, the available ionosonde data are from

Table 1. *Statistics of the reconstructed IED errors of the ASART and the CASART algorithms (unit of the error is* $10^{11}\,el/m^3$*).*

Reconstruction methods	ASART	CASART	IRI 2007
Maximum difference	1.67	0.86	3.25
Minimum difference	–2.14	–1.53	–4.76
Standard deviation	0.74	0.32	1.86

Wuhan station, which locates at 114°E, 30°N. Table 1 shows the comparisons of the reconstructed errors. From table 1, it can be seen that the reconstructed error of the CASART method is smaller than those of the ASART and the IRI 2007 model. The statistic results verify that the CASART is super to the ASART and the IRI 2007 model when it is used to reconstruct the ionospheric electron density distribution.

5. Conclusion and discussion

The CASART method is applied to reconstruct three-dimensional IED distributions using the slant TEC measurements obtained from dual-frequency GPS data. The feasibility of the new algorithm is demonstrated by numerical simulation experiment. The simulation shows that the IED distribution can be reconstructed well when the constraint is suitably selected, and the accuracy of IED reconstruction can be improved. Then the CASART is further used to the IED reconstruction by using the actual GPS observations. The reconstruction results reflect the diurnal variation rules of IED and further confirm the reliability and superiority of the new algorithm.

In the simulated experiment, the slant TECs are obtained using a piecewise constant discretization in the forward model. This is a very important error source, which limits the accuracy of the tomographic reconstruction. In fact, the variability in the ionosphere is continuous rather than discrete, and the measured TECs are integrals, so any kind of discretization will have a certain amount of error associated with it. In the future, it is necessary to investigate a time-varied ionospheric tomography model when the physical sense of the ionosphere is considered.

Acknowledgements

Special thanks are given to Prof. Libo Liu for providing the ionosonde data. This research is supported by the Hunan Provincial Natural Science Foundation for Distinguished Young Scientists (Grant No. 14JJ1021), National Natural Science Foundation of China (Grant No. 41174001), the Research Project of Chinese Ministry of Education (Grant No. 213028A) and the key project of Hunan Education Department (Grant No. 12A0020).

References

Austen J R, Franke S J and Liu C H 1988 Ionospheric imaging using computerized tomography; *Radio Sci.* **23(3)** 299–307.

Escudero A, Schlesier A C, Rius A, Flores A, Larsen G B and Syndergaard S 2001 Ionospheric tomography using Orsted GPS measurements – prelimiary results; *Phys. Chem. Earth* **26(3)** 173–176.

Fredman S V and Nickisch L J 2001 Generalization of ionospheric tomography on diverse data sources: Reconstruction of the three dimensional ionosphere from simultaneous vertical ionograms, backscatter ionograms and total electron content data; *Radio Sci.* **36(5)** 1129–1239.

Gracia R and Crespon F 2008 Radio tomography of the ionosphere: Analysis of an underdetermined, ill-posed inverse problem, and regional application; *Radio Sci.* **43**, doi: 10.1029/2007RS003714.

Kunitsyn V E, Tereshchenko E D, Andreeva E S and Nesterov I A 2010 Satellite radio probing and radio tomography of the ionosphere; *Phys. Usp.* **53(5)** 523–528.

Lee K J and Kamalabadi F 2009 GPS-based radio tomography with edge-preserving regularization; *IEEE Trans. Geosci. Remote Sens.* **47(1)** 312–324.

Li H, Yuan Y B, Li Z S, Huo X L and Yan W 2012 Ionospheric electron concentration imaging using combination of LEO satellites data with ground-based GPS observations over China; *IEEE Trans. Geosci. Remote Sens.* **50(5)** 1728–1735.

Ma X F and Maruyama T 2005 Three-dimensional ionospheric tomogrpahy using observation data of GPS ground receivers and ionosonde by neural network; *J. Geophys. Res.* **110**, doi: 0.1029/2004JA010797.

Mitchell C N and Spencer P S J 2003 A three-dimensional time-dependent algorithm for ionospheric imaging using GPS; *Ann. Geophys.* **46(4)** 687–696.

Nesterov I A and Kunitsyn V E 2011 GNSS radio tomography of the ionosphere: The problem with essential incomplete data; *Adv. Space Res.* **47(10)** 1789–1803.

Persson M, Bone D and Elmqvist H 2001 Total variation norm for three-dimensional iterative reconstruction in limited view angle tomography; *Phys. Med. Bio.* **46(3)** 853–866.

Stoll C, Schluter S, Heise S, Jocobi C, Jakowski N and Raabe A 2006 A GPS based three-dimensional ionospheric imaging tool: Process and assessment; *Adv. Space Res.* **38(11)** 2313–2317.

Thampi S V, Pant T K, Ravindran S, Devasia C V and Sridharan R 2004 Simulation studies on the tomographic reconstruction of the equatorial and low-latitude ionosphere in the context of the Indian tomography experiment: CRABEX; *Ann. Geophys.* **22(10)** 3445–3460.

Wan X H, Zhang F, Chu Q, Zhang K, Sun F, Yuan B and Liu Z Y 2011 Three-dimensional reconstruction using an adaptive simultaneous algebraic reconstruction technique in electron tomography; *J. Struct. Biol.* **175** 277–287.

Wen D B, Yuan Y B, Ou J K, Huo X L and Zhang K F 2007 Three-dimensional ionospheric tomography by an improved algebraic reconstruction technique; *GPS Solut.* **4** 251–258.

Yao Y B, Tang J, Kong J, Zhang L and Zhang S 2013 Application of hybrid regularization method for tomographic reconstruction of mid-latitude ionospheric electron density; *Adv. Space Res.* **52** 2215–2225.

Yizengaw E, Moldwin M B, Dyson P L and Essex E A 2007 Using tomography of GPS TEC to routinely determine ionospheric average electron density profiles; *J. Atmos. Sol.-Terr. Phys.* **69(1)** 314–321.

MS received 8 May 2014; revised 22 August 2014; accepted 25 September 2014